The solid state photo-CIDNP effect

Daviso, E.

Chapter 1

INTRODUCTION

1.1 THEORY OF PHOTO-CIDNP IN SOLIDS

1.1.1 Magnetic field effect

Photosynthetic reaction centres are light-driven electron pumps that convert light energy into chemical energy. Upon photoexcitation, an electron is transferred from two bacteriochlorophylls *a* forming the special pair to a chain of acceptors and a cascade of radical pairs is formed. In a bacterial type II RC, the subsequent ET involves Φ, a bacteriopheophytin *a* coordinated to the L branch of the RC and two quinones Q_A and Q_B. This can be described in the following way

$$P\Phi Q_A Q_B \rightarrow P^{*}\Phi Q_A Q_B \rightarrow P^{+\bullet}\Phi^{-\bullet} Q_A Q_B \rightarrow P^{+\bullet}\Phi Q_A^{-\bullet} Q_B \rightarrow P^{+\bullet}\Phi Q_A Q_B^{-\bullet}.$$

The kinetics of the ET decreases at each step. In *Rb. sphaeroides*, the first ET step takes place within 3 ps. The final step from Q_A to Q_B occurs in 60-100 μs (for review, see Hoff and Deisenhofer, 1997). When the ET to Q_A is blocked, the lifetime of $P^{\cdot+}\Phi_A^{\cdot-}$ increases ca. 100-fold for the singlet radical state S (to ~20 ns) and for the triplet radical state T_0 (to ~1 ns), allowing for evolution under hyperfine interaction between the electron pair and nuclei (Figure 1.1). Hyperfine interactions and the difference of the electron Zeeman interactions of the two radicals become evident by interconversion of the singlet-born spin-correlated radical pair to the triplet state. When the magnetic field effect on the triplet yield was discovered in bacterial RCs (Blankenship *et al.*, 1977; Hoff *et al.*, 1977a), the connection to the photochemically induced dynamic electron polarization (CIDEP), which had been discovered shortly before in chloroplasts (Blankenship *et al.*, 1975) and RCs of purple bacteria (Hoff *et al.*, 1977b), has been made immediately. Both, the triplet yield and CIDEP were traced back to magnetic-field dependent interaction of electrons with nuclei (Hoff *et al.*, 1977a; Werner *et al.*, 1978; Hoff, 1984). Based on this interpretation, "new classes of experiments" were foreseen (Goldstein and Boxer, 1987), although the exact mode of electron-nuclear polarization transfer was not known yet.

Photo-CIDNP is well-known from liquid NMR (for review, see Hore and Broadhurst, 1993; Goez, 1997) where it has been observed for the first time in 1967 (Bargon *et al.*, 1967; Bargon and Fischer, 1967; Ward and Lawler, 1967). Soon, it was

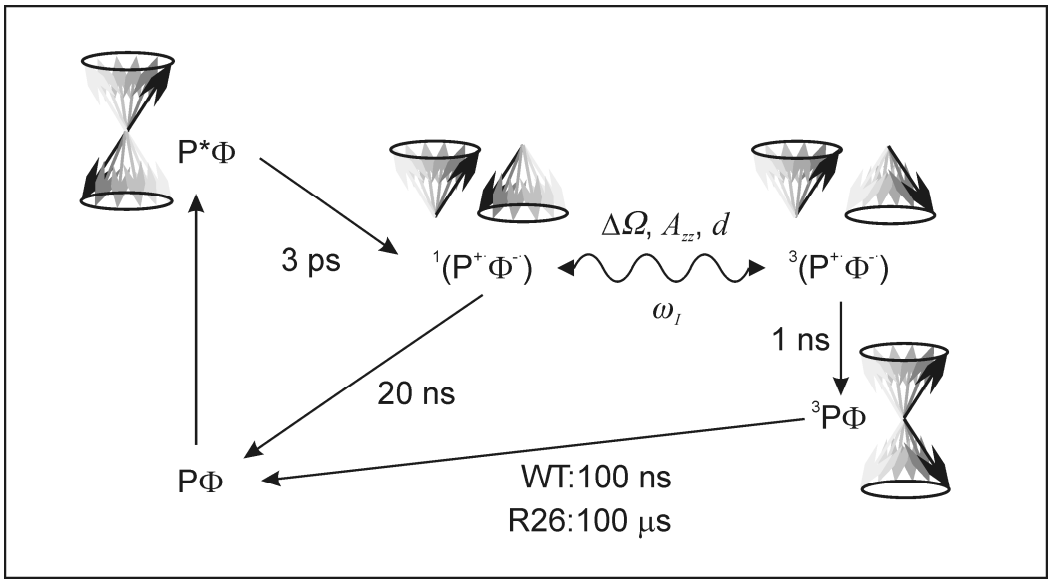

Figure 1.1: Kinetics and spin dynamics of the electron transport in quinone-blocked RCs of *Rb. sphaeroides* wild-type and the carotenoid-less strain R26. After light-absorption, from the photochemically excited state of the primary donor P*, an electron is transferred to the primary acceptor Φ, a bacteriopheophytin cofactor attached to the L branch of the protein. This radical pair is born in a pure singlet state $^1(P^{+\bullet}\Phi^{-\bullet})$. The singlet radical pair evolves into a triplet radical pair $^3(P^{+\bullet}\Phi^{-\bullet})$ with a frequency that depends on the hfi (A_{zz}), the difference of the electron Zeeman frequency ($\Delta\Omega$) and the electron-electron coupling (d). The probability that the radical is in a singlet or triplet state depends on the sign of the nuclear Zeeman frequency (ω_I). Concomitantly to this process of spin intersystem crossing, electronic coherence is converted into nuclear polarization by the three-spin mixing (TSM). In the differential decay (DD) mechanism, a net photo-CIDNP effect is established if spin-correlated radical pairs have different lifetimes in their singlet and triplet states. An electron back-transfer leads to the initial electronic ground-state. In RCs having a long lifetime of the donor triplet, as in R26 RCs, the differential relaxation (DR) mechanism occurs since nuclear spin relaxation is significant on the triplet branch causing incomplete cancellation of nuclear polarization of both branches.

explained by the radical-pair mechanism (Closs and Closs, 1969; Kaptein and Oosterhoff, 1969) which also inspired the interpretation of the electron-nuclear interaction in RCs (Haberkorn and Michel-Beyerle, 1979; Haberkorn *et al.*, 1979; Boxer *et al.*, 1983).

In 1994, Zysmilich and McDermott observed for the first time the solid-state photo-CIDNP effect in RCs, applying magic angle spinning NMR at low temperature to uniformly ^{15}N-labeled quinone-blocked bacterial RCs of *Rb. sphaeroides* R26 (Zysmilich and McDermott, 1994). This solid-state photo-CIDNP effect has indeed been shown to be field dependent (Figure 1.2) (Prakash *et al.*, 2005a). Using the signal from about 3300 methyl groups of the entire bacterial RC at 31 ppm as internal standard, enhancement factors of 60 (17.6 Tesla), 1000 (9.4 Tesla) and about 10000 (4.7 Tesla) were observed.

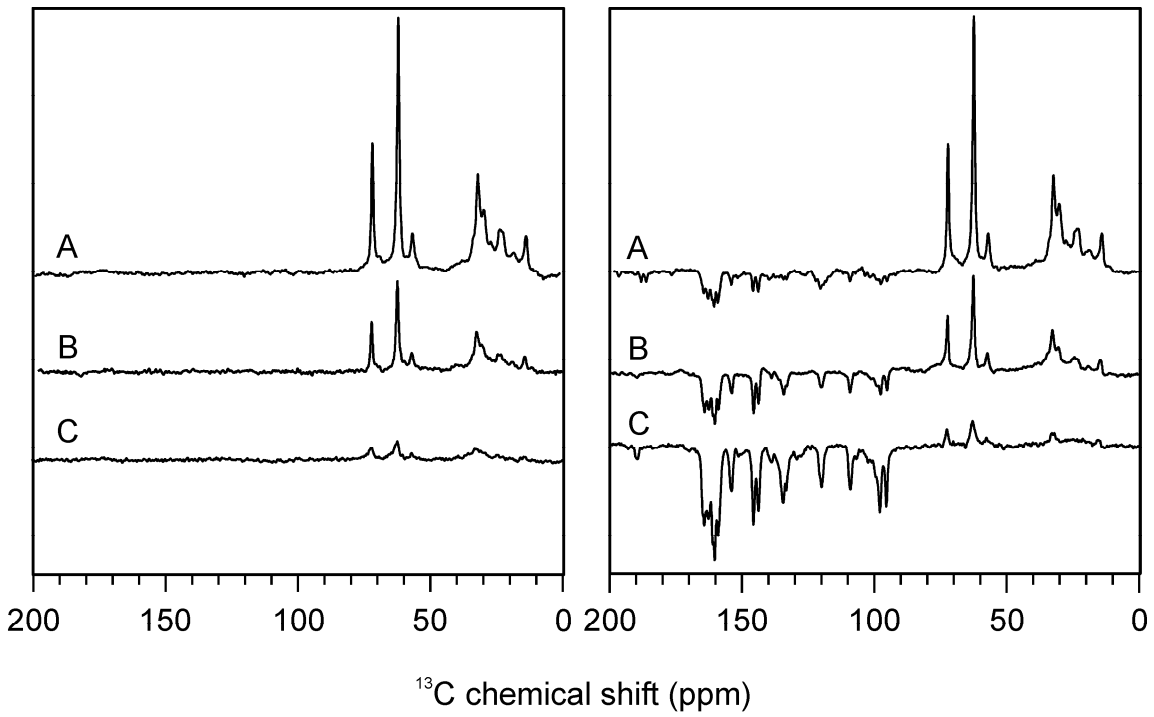

Figure 1.2: ^{13}C MAS NMR spectra of quinone depleted RCs of *Rb. sphaeroides* wild type obtained in the dark (left) and under continuous illumination with white light (right) at different magnetic fields at 17.6 T (A), 9.4 T (B) and 4.7 T (C). Sample temperature was 223 K and a MAS rotational frequency of 8 kHz was used.

The relevant enhancement factor increases selectivity and sensitivity in solid-state NMR, enabling the new classes of experiments foreseen by Goldstein and Boxer (1987).

1.1.2 Primary sources of enhanced nuclear magnetization

The origin of photo-CIDNP in solution state is described by the RPM. In this process both the A_{zz} element of the secular hyperfine coupling and the $\Delta\Omega$ mediate spin intersystem crossing (ISC) to the T_0. During ISC, the RPM acts as a nuclear spin sorting mechanism in which a nuclear spin polarization with the same magnitude but opposite sign is induced in the S manifold compared to the T_0 manifold. The two different products would cancel out if the chemical fate of the S and the T_0 products is the same. Since the RPM depends also on diffusion, it cannot be the explanation for the solid-state photo-CIDNP effect in frozen RCs. For the photo-CIDNP effect in solids under continuous illumination, several new mechanisms have been proposed (Figure 1.1) (for a recent discussion, see Jeschke and Matysik, 2003).

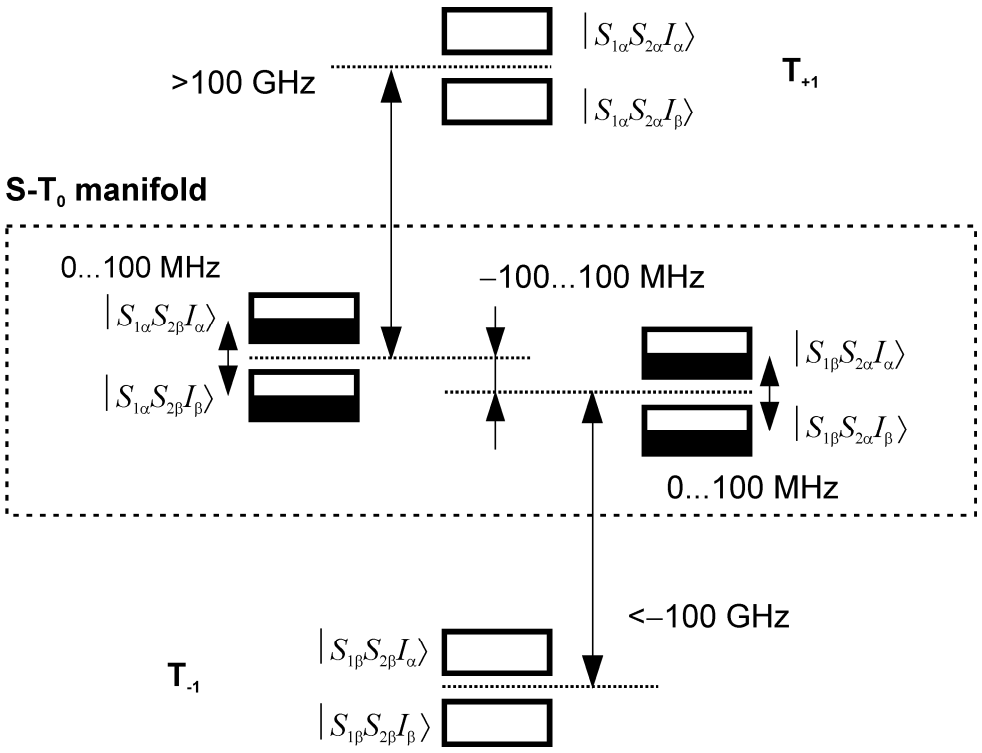

Figure 1.3: Energy levels of the radical pair in bacterial RC. At thermal equilibrium, all four electron spin states in a correlated radical pair (S, T_0, T_{+1} and T_{-1}) would be populated according to the Boltzmann distribution with the nuclear levels equally populated as indicted by the black-white boxes in the figure. Immediately after radical pair formation, only the S state is populated. This initial state is a non stationary state that allows for coherent interconversion between the S and the T_0 states. The four quantum states of the S-T_0 manifold are split due to the difference of the Zeeman interaction of both electrons spin, the hyperfine coupling to the nuclear spin, the nuclear Zeeman interaction, and the coupling between the two electron spins. The values are magnetic field dependent; in this picture a field of 9.4 T is considered.

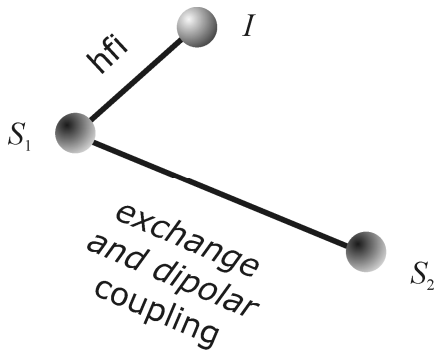

Figure 1.4: The electron-electron-nuclear model system and the interactions occurring in the TSM process. For the DD mechanism only electron-nuclear interaction is required. The interaction between electron S_1 and nucleus I, which may lead to a degeneracy of quantum states of the S-T_0 manifold, is described by the pseudosecular part B of the hfi. This introduces orientation dependence into the magnitude and sign of photo-CIDNP. The interactions between the two electrons are exchange coupling J and dipolar coupling ω_{dd}.

1.1.3 Three spin mixing

Photo-induced ET in the RC leads to a SCRP. The initial radical pair is born in a pure S state (Figure 1.3). During the lifetime of the radical pair, the system oscillates between the S and the T_0 states having magnetic quantum number $m = 0$.

The evolution from the S to the T_0 state and from T_0 back to the S state is accompanied by a transfer of fictitious electron polarization to the nuclei (Jeschke, 1997). The relevant parameters that drive the ISC are the secular part of the hf interaction, the difference of the electron Zeeman between the two electrons and the coupling between the two electrons (Figure 1.4, see also Jeschke and Matysik, 2003).

Net nuclear polarization is generated in the SCRP due to the presence of both the pseudosecular parts of the hf interaction (A_{zx}, A_{zy}) and the coupling between the two electron spins (d) (Figure 1.5). The electron-electron-nuclear model system for three spin mixing (TSM) consists of two electron spins $S_1 = ½$, $S_2 = ½$, and one nuclear spin $I = ½$. A product operator basis for the S-T_0 subspace is constructed from operators of the nuclear spin $I = ½$ and of a fictitious electron spin $S' = ½$, with the fictitious spin corresponding to the zero-quantum transition of the two electron spins in the S-T_0 manifold. Correspondence rules between spin operators of the two coupled spins S_1 and S_2 and of the fictitious electron spin S' have been given elsewhere (Jeschke, 1997). The fictitious density matrix at the instant of the radical pair formation is in a pure singlet state and is given by

$$\sigma_{\mathrm{S}} = \frac{1}{2} E_{S'} - S_x', \tag{1.1}$$

where E is the identity operator and $-S_x'$ is the operator describing the fictitious electron spin polarization. The Hamiltonian for the S-T_0 subsystem (Jeschke and Matysik, 2003) is

$$\mathrm{H}_{\mathrm{ST}_0} = \Delta\Omega S_z' + \omega_I I_z + A_{zz} S_z' I_z + A_{zx} S_z' I_x + A_{zy} S_z' I_y - d S_x'. \tag{1.2}$$

Here the $\Delta\Omega$ is the electron Zeeman interaction, ω_I is the nuclear Zeeman interaction, A_{zz} represents the secular hf coupling and A_{zx} and A_{zy} are the pseudosecular hf couplings and $d = 2J + d'$ is the total coupling between the two electron spins, with J the exchange coupling and d' the dipole-dipole coupling (see also Appendix A). A maximum of net nuclear polarization through the TSM is generated when one of the double matching conditions is fulfilled

$$2|\Delta\Omega| = 2|\omega_I| = |A_{zz}|, \tag{1.3}$$

$$2|d| = 2|\omega_I| = |A_{zz}|. \tag{1.4}$$

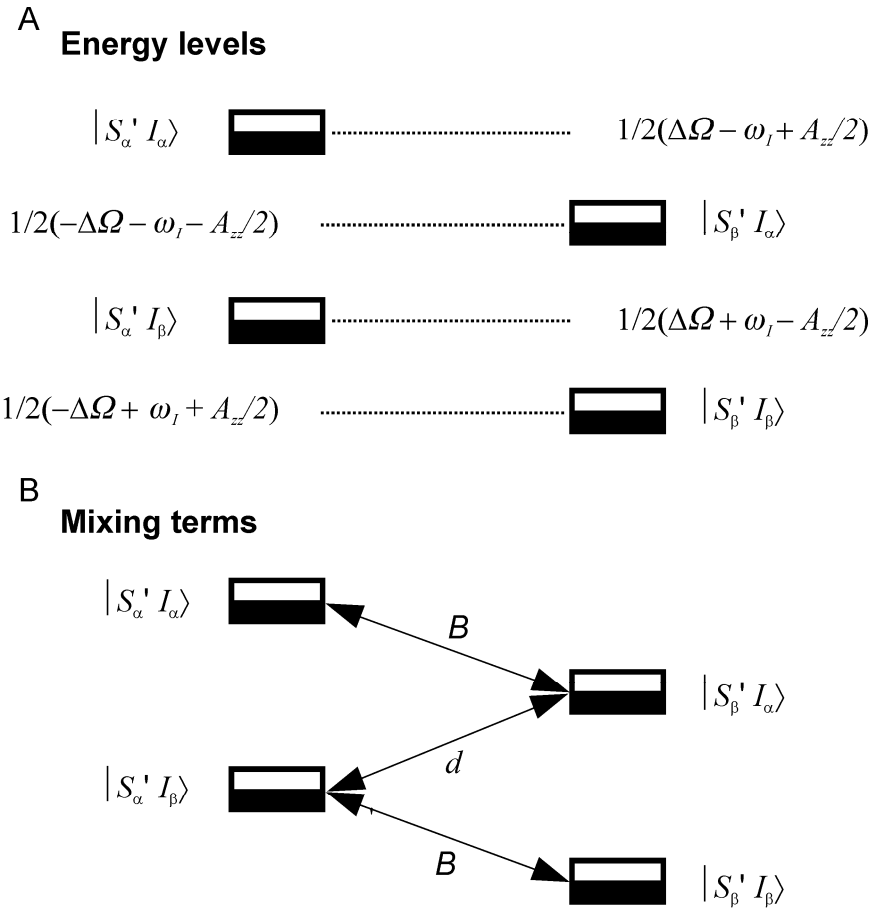

Figure 1.5: (A) Energy levels and mixing terms allowing electron-electron-nuclear three-spin mixing. The four quantum states of the S-T_0 manifold are split due to the difference of the Zeeman interaction of the radical pair, the hyperfine coupling to the nuclear spin, the nuclear Zeeman interaction, and the coupling between the two electron spins. (B) The mixing of the states is caused by the absolute pseudosecular contribution *B* as well as the electron-electron coupling *d*.

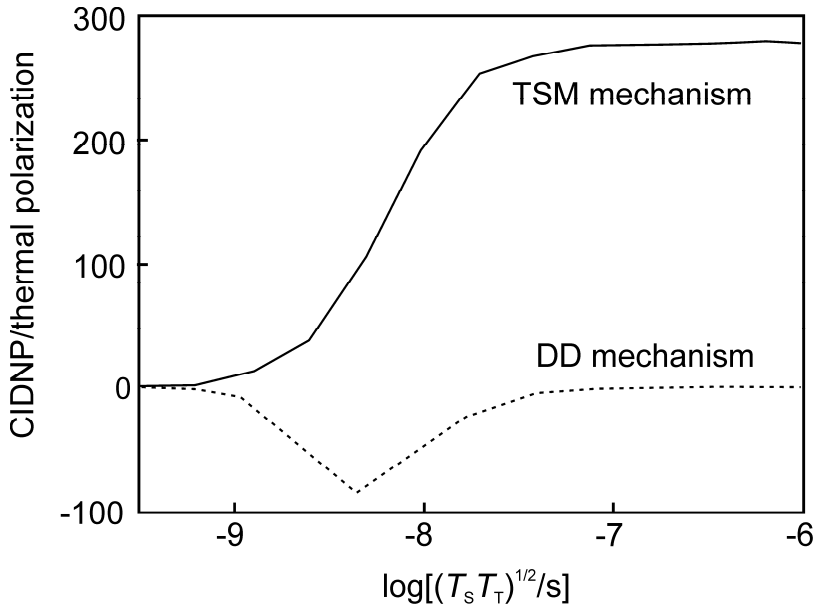

Figure 1.6: ^{13}C photo-CIDNP effects on the lifetime of the radical pair calculated for a single orientation. Lifetime dependence of only the TSM contribution (if $T_S = T_T$) and only the DD contribution ($T_S/T_T = 20$, $d = 0$). For more information see Jeschke and Matysik, 2003.

In RCs of *Rb. sphaeroides*, none of the double matching conditions (Equations 1.3 and 1.4) are well fulfilled by the radical pair but the strongest nuclear polarization is obtained when the applied magnetic field is between 2 and 5 T. At other fields and orientations the situation may be different. For both matching conditions, the three states $\left|S_\alpha', I_\beta\right\rangle$, $\left|S_\beta', I_\alpha\right\rangle$ and $\left|S_\beta', I_\beta\right\rangle$ in the S-T_0 manifold have the same energy, but initially also have equal populations (Figure 1.5). The *d* mixes two of the states and thus creates coherent evolution of the fictitious electron spin S' whose sign depends on the sign of *d*. The orientation dependence of d' is given by $d' = 1/2D(3\cos^2\theta - 1)$, where θ is the angle between the spin-spin-vector and the external magnetic field and *D* the magnitude of the dipolar coupling (see Appendix A). The absolute pseudosecular contribution $B = \sqrt{\left(A_{zx}^2 + A_{zy}^2\right)}$ mixes one of the states affected by the *d* term with the third state, so that the fictitious electron polarization is transferred to nuclei. The TSM contribution vanishes at the canonical orientation of the hf tensor where *B*= 0, while it persists for $\Delta\Omega = 0$ or $A_{zz} = 0$. The polarization transfer is maximum when $\Delta\Omega = 0$. The TSM mechanism creates significant polarization only if the product of the electron-electron coupling *d* and the radical pair lifetime is of the order of unity or larger. On the other hand, the contribution also vanishes if *d* is so large that the S and the T_0 states become eigenstates of the pair. TSM contributions are thus observed only for moderate electron-electron couplings.

1.1.4 Differential decay

In the Differential Decay (DD) mechanism, photophysics and spin dynamics work together to build up polarization. Instead of the electron-electron coupling *d*, the different lifetimes T_S of the S and T_T of the T_0 affect the polarization of the fictitious spin S'. As in the TSM mechanism, the pseudosecular part *B* of the hf interaction converts the fictitious electron spin polarization to net nuclear polarization. The DD mechanism thus persists when $d = 0$ but vanishes when $\Delta\Omega = 0$ and $A_{zz} = 0$.

The DD mechanism requires only a single matching of interactions,

$$2\left|\omega_I\right| = \left|A_{zz}\right|. \tag{1.5}$$

The time scale of radical pair decay, $(T_S T_T)^{1/2}$, is related to the decay time constant of recombination of the singlet radical pair to the ground-state T_S and the formation of the donor triplet (T) from the triplet radical pair T_T. The efficiency of the DD mechanism

depends on a matching of the time scale of $\Delta\Omega$ or hf-induced ISC with this time scale of radical pair decay. This is shown in Figure 1.6, which has been computed for a single orientation. After implementation of powder averaging, a predominant DD contribution causes positive signals, while negative signals originate from a predominant TSM contribution (Jeschke, personal communication). This observation is in line with simulations as well as observations of ^{15}N photo-CIDNP and the temperature dependence of ^{13}C photo-CIDNP. Hence, the observed NMR envelope for the steady state is a superposition of dark signals and photo-CIDNP signals produced by two competing mechanisms. The same conclusion has been made for ^{13}C photo-CIDNP in photosystem I (PSI).

1.1.5 Differential relaxation

In the Differential Relaxation (DR) mechanism the opposite polarization from the S and the T_0 does not cancel since part of the triplet-derived polarization relaxes during the lifetime of the T (McDermott *et al.*, 1998). This requires that the longitudinal relaxation time of the nuclei in the T is shortened to such an extent that it is comparable to the triplet lifetime. The contribution of the DR mechanism to photo-CIDNP is difficult to predict since nuclear longitudinal relaxation times in the T state are not known. However, as pointed out by Jeschke (1998) as well as Polenova and McDermott (1999), the observation of photo-CIDNP on the bacteriopheophytin acceptor (Zysmilich and McDermott, 1996; Schulten *et al.*, 2002) can hardly be explained by the DR. In addition, a dramatic decrease of the DR contribution would be expected for WT (T lifetime of 100 ns) compared to R26 (T lifetime of 100 µs). Assuming that nuclear relaxation times are the same in WT and R26 triplets, the DR mechanism is thus negligible for WT bacterial RCs. However, the difference in polarization patterns between WT and R26 RCs can be explained by a DR contribution. The observed sign change for signals that were assigned to P would be in line with such an explanation and the implied dependence of the nuclear spin relaxation times on the hf couplings is in line with the expected efficiency of paramagnetic relaxation (Prakash, 2006).

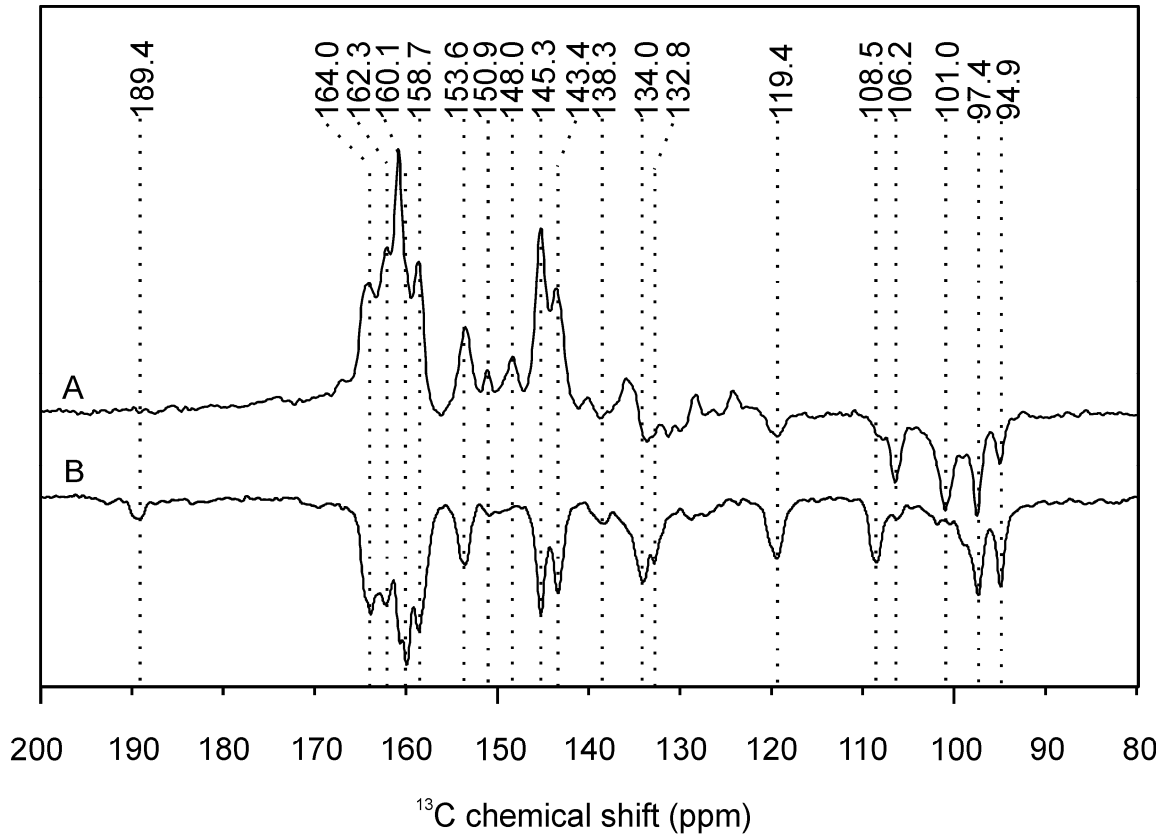

Figure 1.7: Comparison of ^{13}C photo-CIDNP MAS NMR spectra obtained from purified RCs of *Rb. sphaeroides*. (A) Carotenoid-less mutant strain R26. (B) Wild type collected under continuous illumination.

1.1.6 Donor excited triplet state

Due to the absence of a carotenoid cofactor close to P in the R26 mutant, the lifetime of the T increases to 100 μs compared to 100 ns in WT (Figure 1.1). The ^{13}C photo-CIDNP MAS NMR spectrum of R26 shows similar intensities as that of WT, however, the sign of the donor signals is inverted (Figure 1.7) (Prakash *et al.*, 2006). This effect could be rationalized either by the DR mechanism or by significant back-transfer from the long-lived ^{3}P state into the radical pair (Chidsey *et al.*, 1985). Such triplet-born radical-pairs undergo TSM and DD like singlet-born radical pairs, however the sign is inverted. Simulations indicate, however, that back-transfer would lead to a sign change for both acceptor and donor signals, while the DR contribution inverts the sign of only the donor signals, in better agreement with observations.

1.2 CONTINUOUS ILLUMINATION PHOTO-CIDNP IN SOLIDS

1.2.1 Steady state build-up

Figure 1.8 shows the accumulation of light induced nuclear polarization to the steady state of *Rb. sphaeroides* R26 (Prakash *et al.*, 2005b).

Each point on the curve gives the ratio of intensities of the peak at 161 ppm (I_{161}) to the peak of the backbone signal at 31 ppm (I_{31}) at different light pulse durations. A fit by first-order build-up kinetics $I_{161}/I_{31} = 1-\exp(-kt)$ results in $k = 0.235\ s^{-1}$. A minor initial intensity of 0.067 is present in the dark. It is caused by aromatic carbons in the dark and has been subtracted prior to fitting. The steady-state photo-CIDNP signal collected with continuous illumination reaches 50% of the total signal intensity in about 3s. After ~10 s, the signal level is 90% of the steady state. For comparable experimental conditions, an average value of 50 turnovers per second per RC has been estimated previously (Matysik *et al.*, 2001a). Hence, the steady state is reached after the absorption of ~500 photons per RC.

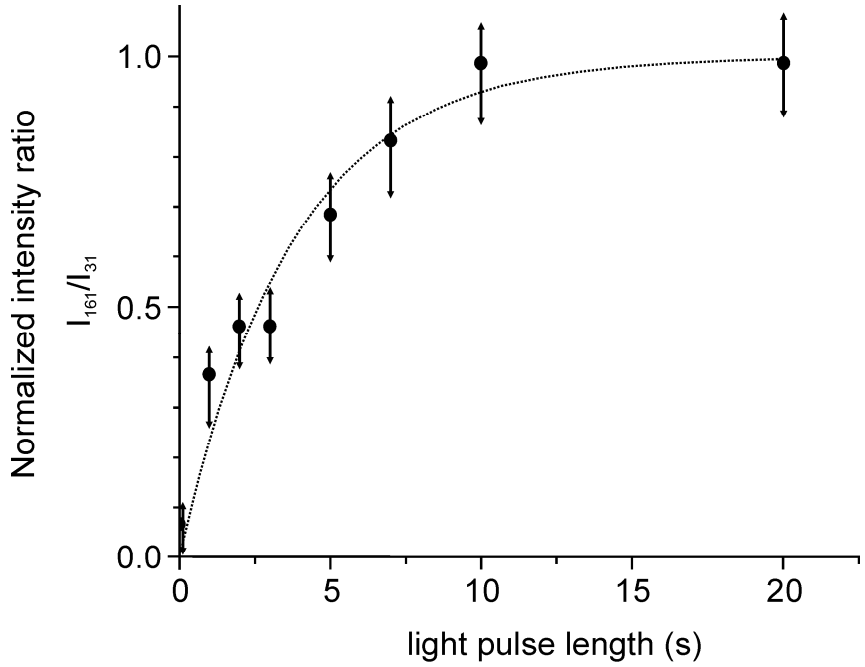

Figure 1.8: The build-up curve of ^{13}C photo-CIDNP to the steady state as a function of the light pulse length. The ratio normalized ratio of the intensity of the light-induced signal at 161 ppm to the dark signal at 31 ppm approaches saturation at about 10 seconds of continuous illumination.

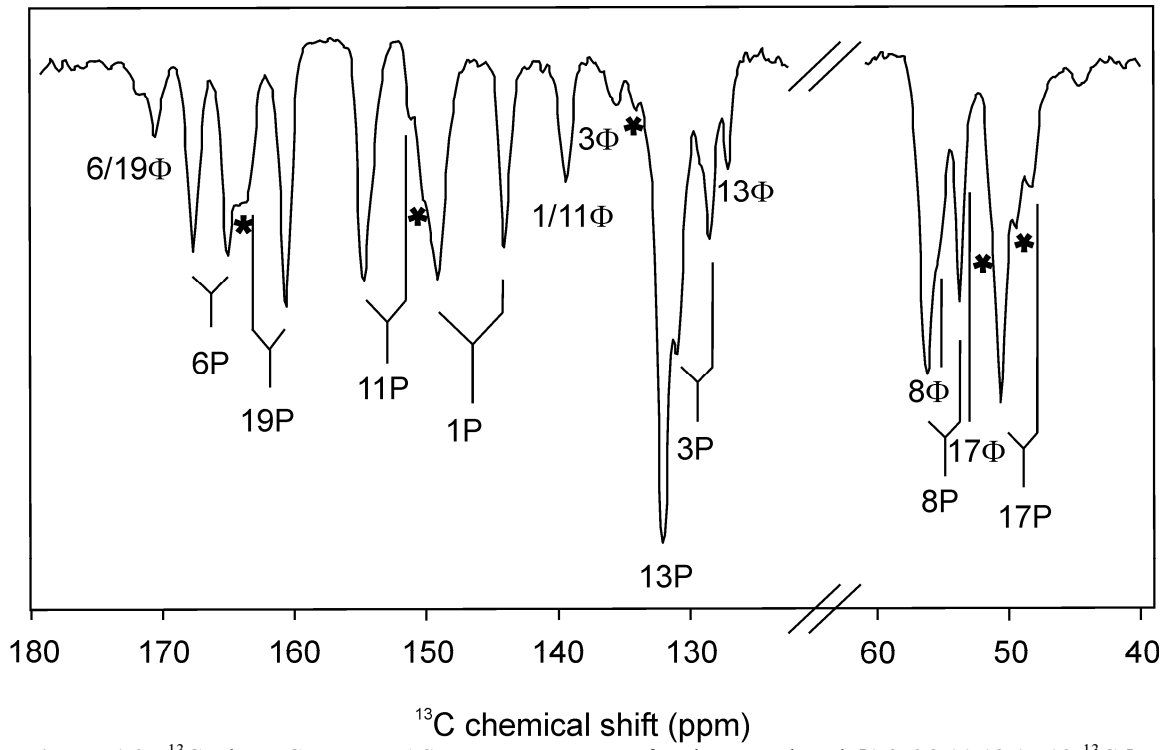

Figure 1.9: ^{13}C photo-CIDNP MAS NMR spectrum of quinone-reduced [1,3,6,8,11,13,17,19-$^{13}C_8$]-BChl/BPhe labeled bacterial RC wild type collected with continuous illumination at 9.4 T. The label P identifies resonances assigned to the donor P. The label Φ identifies resonances assigned to the bacteriopheophythines coordinated to the L branch. Sidebands are marked with an asterix (Schulten *et al.*, 2002).

1.2.2 Polarization transfer between nuclei

In steady-state experiments on selectively ^{13}C isotope-labeled RCs, transfer of nuclear polarization to nuclei in close vicinity and concomitant equilibration of signal intensity have been observed (Figure 1.9) (Matysik *et al.*, 2001b). On the one hand, such a secondary effect hides the true photo-CIDNP intensities; on the other hand, it allows exploring neighboring atoms selectively depending on the chosen label pattern. Polarization transfer into the protein matrix has also been observed in 4'-^{13}C-Tyr-labeled bacterial RCs (Matysik *et al.*, 2001a). Hence, a molecule providing photo-CIDNP can be applied as a "spin-torch" in solid-state NMR to explore cavities and surfaces. By analogy to transfer of ^{13}C polarization between domains in polymer materials (Robyr *et al.*, 1995), this transfer process is most likely due to proton-driven spin diffusion which would imply a through-space transfer mediated by dipole-dipole couplings between $^{13}C \rightarrow {}^{1}H \rightarrow {}^{1}H \rightarrow {}^{13}C$.

For pairs of ^{13}C nuclei that are separated only by one to three bonds and whose shift difference is not much larger than the expected *J* coupling experienced by the nuclei,

corresponding to a few ppm, direct ^{13}C-^{13}C through-bond polarization transfer could be feasible.

1.3 SIMULATIONS

Numerical simulations of the photo-CIDNP effect are based on the theory described in Jeschke and Matysik (2003), implemented in the Matlab program (G. Jeschke, unpublished) for density matrix computation using the EasySpin library (Stoll, 2003). The program starts from the density matrix in a pure S state (Equation 1.1) and computes the time evolution of the system using the Hamiltonian (Equation 1.2) that includes electron Zeeman, nuclear Zeeman and hfi as well as dipole-dipole and exchange coupling between the two electron spins. The part of the density matrix that represents decay channels from either the S to the ground state or from the T_0 to the T is projected out and is further evolved using a Hamiltonian including only the nuclear Zeeman interaction.

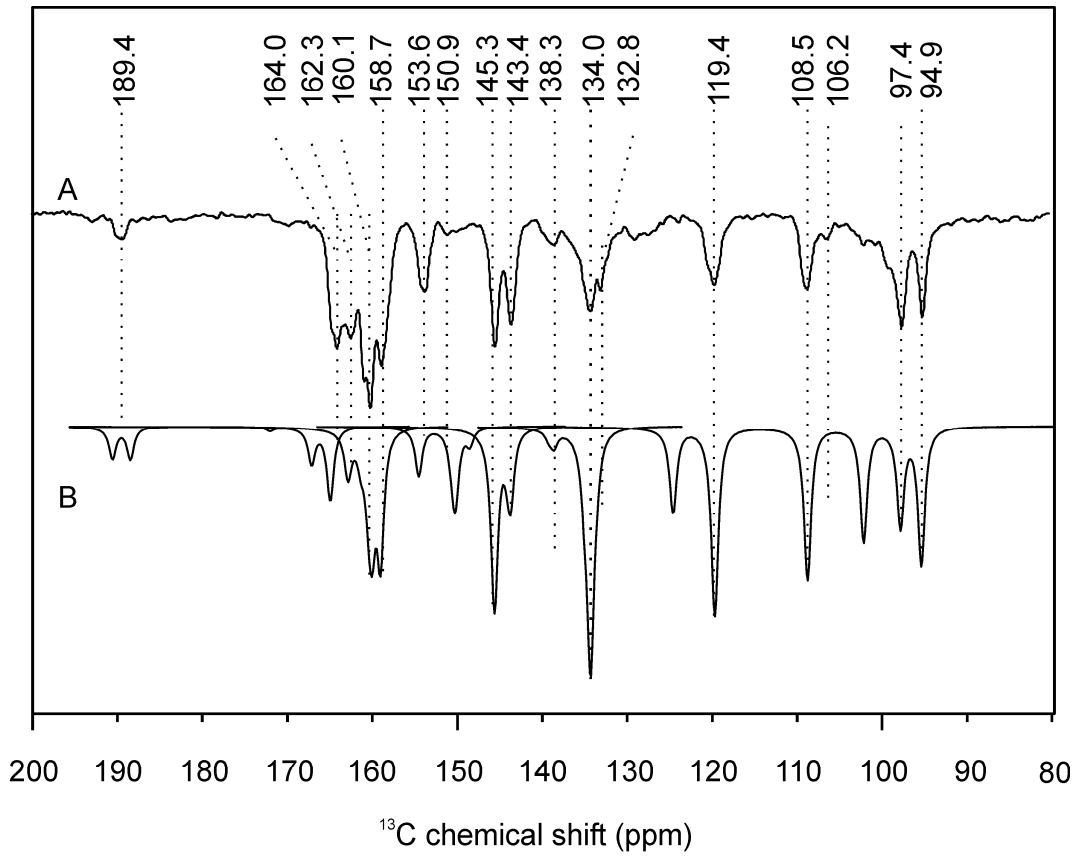

Figure 1.10: (A) ^{13}C MAS NMR spectra RC of *Rb. sphaeroides* wild type obtained at 4.7 T and 223 K under continuous illumination. (B) Simulation of the photo-CIDNP polarization pattern. The set of parameters used for (B) such as the hf tensors of the ^{13}C nuclei, the electron-electron dipolar tensor, the *g* tensor of the radicals and the exchange parameter are reported in Appendix A.

In pure RCs of *Rb. sphaeroides* WT, evolution is continued until the radical pairs have completely decayed (100 ns) and after that the nuclear polarization of the diamagnetic part of the density matrix is determined. As an extension to the approach described by Jeschke and Matysik (2003), this procedure is performed for a full powder average, describing all interactions by tensors, except for the nuclear Zeeman interaction whose anisotropy is negligible on a time scale of 100 ns. Nuclear polarization was normalized to the thermal polarization at the measurement temperature of 223 K and chemical shift values for simulating photo-CIDNP spectra have been compiled in Prakash *et al.* (2005a). The absolute value of nuclear polarization has been used in the input file of SIMPSON. For the SIMPSON simulation, a script for a spin echo sequence was written that implemented the same sixteen-step phase cycle (CYCLOPS and cycling of the (π) pulse) as used in the experiments (see Appendix B). The simulated spectra of each resonance have been superimposed using SIMPLOT (Figure 1.10). Despite the difference in magnitude for the peak at 134.0 ppm assigned to ^{13}C-2 of the Φ (Prakash, 2006), the good coincidence between experimental and calculated ^{13}C photo-CIDNP intensities suggests that the continuous illumination ^{13}C-photo-CIDNP MAS NMR spectrum can be understood in terms of a superposition of contributions from the TSM and DD mechanisms for WT where the lifetime of the T is limited to 100 ns. Analogous simulations predict maximum enhancements for ^{1}H as small as 2-3 times thermal polarization. This would provide a possible reason why attempts to detect both liquid and solid-state photo-CIDNP on ^{1}H failed.

1.4 PHOTO-CIDNP MAS NMR SET-UP

1.4.1 Continuous illumination setup

The continuous light illumination setup for MAS NMR experiments comprises a 1000-Watt xenon arc lamp with collimation optics, a liquid filter and glass filters, a focusing element and a light fibre (Figure 1.11). Since the emission spectrum of a Xe lamp is similar to sunlight, the full range of radiation from UV to IR is available for illumination.

Disturbance of the spinning frequency counter, working in the near-IR region by the incident radiation, is avoided by various liquid and glass filters. A fibre bundle is used to transfer the radiation from the collimation optics to the sample.

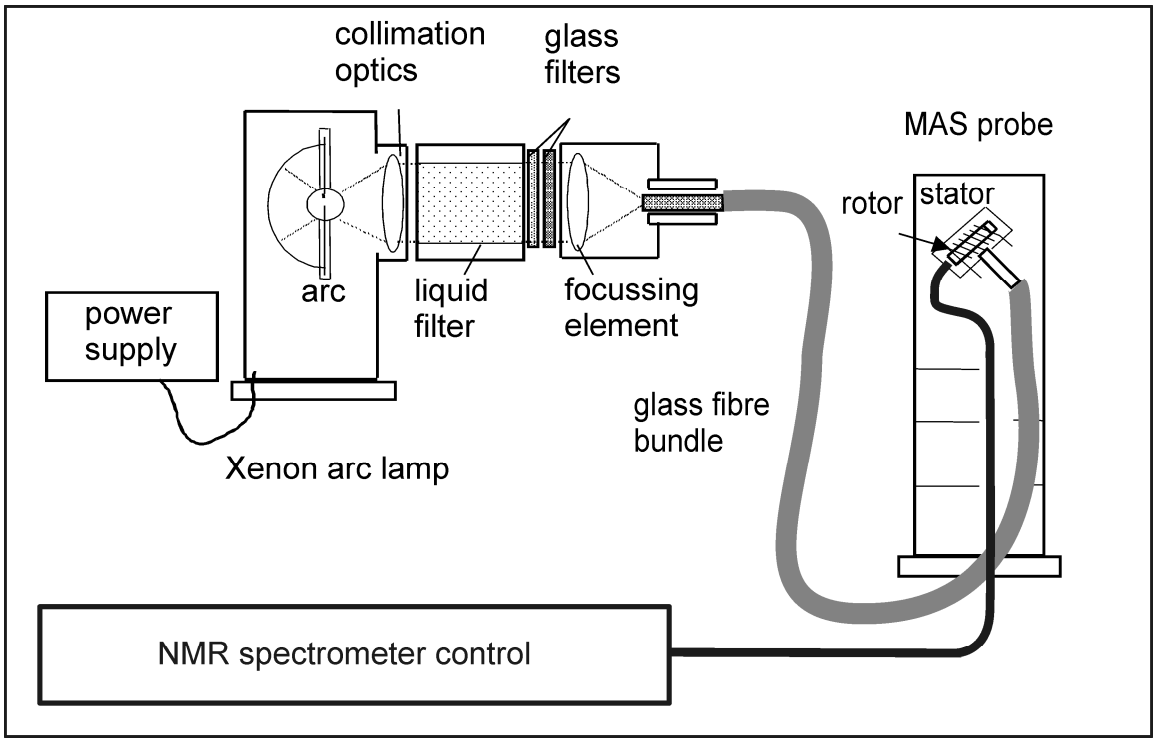

Figure 1.11: Setup for the detection of continuous illumination photo-CIDNP. The setup is based on a 1000-W Xenon lamp, condenser optics and filters. Light is transferred by a multimode fibre bundle into the probe.

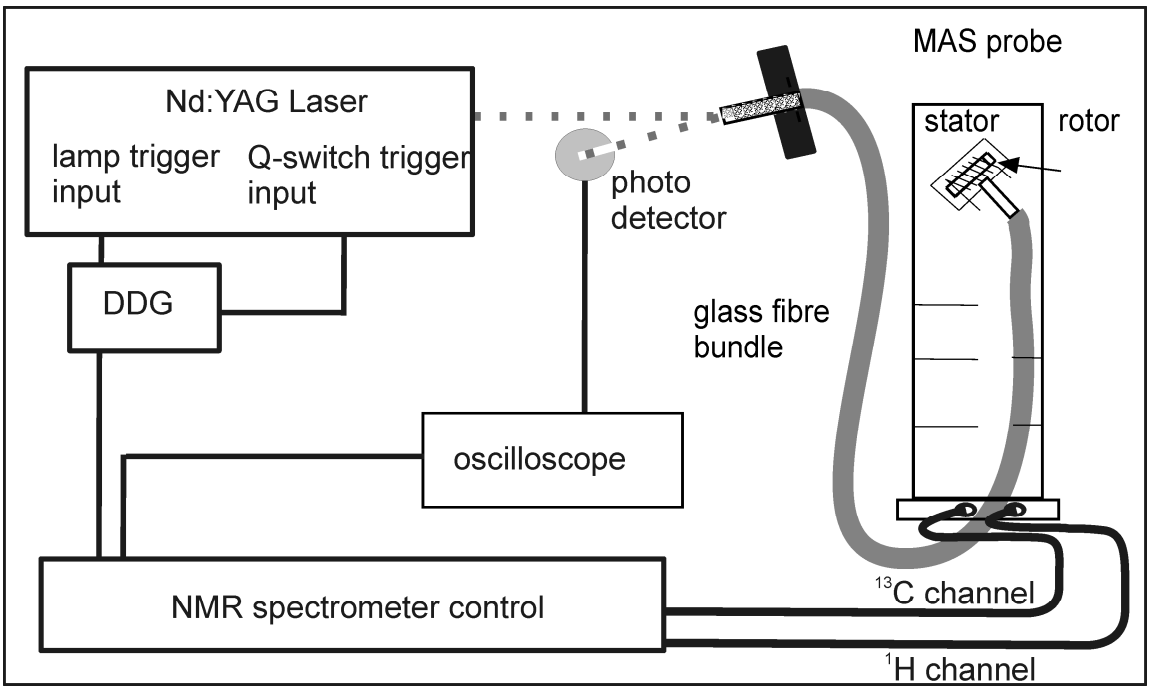

Figure 1.12: Setup for the detection of laser pulsed photo-CIDNP. A digital delay generator connects the NMR spectrometer console to the laser. Laser flashes are transferred by a fibre bundle into the probe. Radiation reflected at the surface of the fibre aperture is measured by a photodetector in order to check the performance of the laser during the experiment.

A multi-mode light fibre bundle provides high optical transparency in a broad spectral range, as well as sufficient mechanical flexibility for being attached to the stator of the MAS probe. The MAS probes have been modified in order to illuminate the rotor from the side. This includes (a) a bore drilled into the most upper partition plate separating stator chamber and electronics, (b) drilling a small opening into the stator, and (c) winding a new coil from thin silver wire. The samples have been loaded into optically transparent sapphire rotors to ensure homogeneous illumination. Furthermore, a mechanical shutter can be easily incorporated into the setup, allowing for studies of build-up kinetics and spin-diffusion theoretically down to microsecond resolution. However, the photon rates achieved with a Xenon arc lamp are not sufficient to induce observable photo-CIDNP effects on time scales much shorter than a second.

1.4.2 Laser setup

Additional improvement of time-resolution requires much higher photon rates and thus a laser setup. A nanosecond laser provides sufficient intensity for photo-CIDNP MAS NMR studies. Such a setup comprises a laser with 15 Hz repetition rate at 532 nm, a digital delay generator (DDG), a fibre aligner and a multimode optical light fibre (Figure 1.12). The pulse width can be short as 6-8 ns. A DDG triggers both the pump lamp, exciting the Nd:YAG crystal, and the laser Q-switch. The NMR spectrometer generates the triggering impulse for the DDG via NMR pulse programming. As determined by experiments with various Schott glass filters, green light produces the strongest photo-CIDNP effect since it penetrates deep into the optically very dense sample. The timing can be checked using a 500-MHz oscilloscope connected to the channel of the spectrometer that triggers the ^{13}C pulse and to a home-made photodetector.

The photodetector consists of a fast photodiode (FND-100, EG&G, Salem, USA) connected to an amplifier. The timing precision of the combined optical and NMR experiment is approximately ±10 ns (Figure 1.13). Note, however, that the time resolution of photo-CIDNP experiments is limited by the length of the (π/2) radiofrequency (rf) pulse used for NMR excitation. Detection of photo-chemically induced nuclear coherence, if feasible, would overcome this limitation of time resolution. The laser set up is described in more detail in Chapter 2.

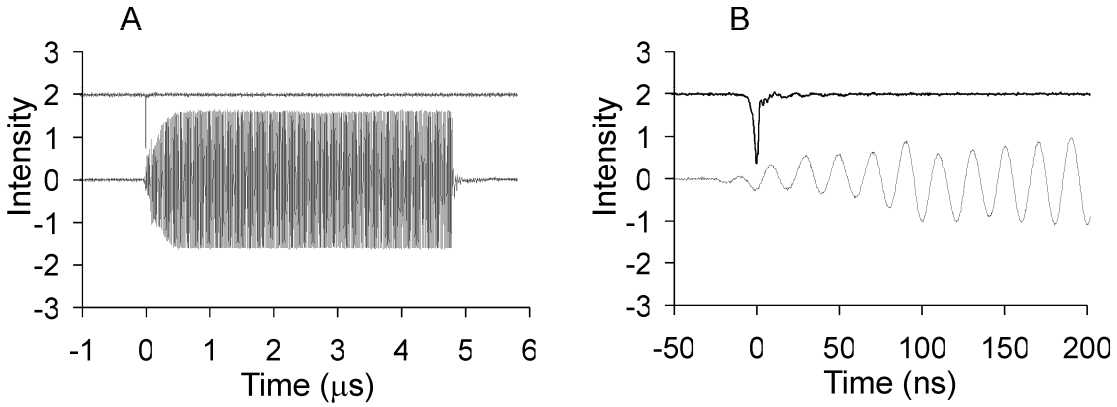

Figure 1.13: (A) laser light pulse signal (top) and the π/2 ^{13}C NMR pulse (bottom). The length of the NMR pulse is exactly 4.85 μs. (B) Detailed view at the leading edge of the laser light pulse (top) and the π/2 ^{13}C NMR pulse (bottom). The width at half height of the light pulse is 8 ns.

1.4.3 Pulse sequences

Standard steady-state photo-CIDNP MAS NMR spectra are collected using continuous illumination by recording Bloch decays induced by the spin-echo pulse sequence and with two-pulse phase modulation (TPPM) proton decoupling (Bennett *et al.*, 1995).

Depending on the static magnetic field, cycle delays from 4 to 15 s are used. In nanosecond laser flash experiments, primary polarization is weaker than for the steady state and sensitivity is too low for detection with such long recycle delays. Application of a ^{13}C presaturation pulse destroys any polarization from previous laser flashes that is still present before the laser pulse (see Chapter 2). The recycle delay can be thus reduced to the instrumental limit of the NMR console, which is ~200 ms. With the same equipment, the length of the (π/2) carbon pulse, determined on uniformly ^{13}C labeled tyrosine, can be optimized from 4 and 5 μs a rf power of ~250 W (Figure 1.13A).

Established multidimensional pulse sequences, for example for radio-frequency driven dipolar recoupling (RFDR) experiments (Gullion and Vega, 1992; Boender and Vega, 1998; Bak *et al.*, 2000), can be applied to photo-CIDNP pulse schemes by exchange of the initial cross polarization transfer by a direct (π/2) carbon pulse.

1.5 APPLICATIONS

1.5.1 Electronic structure of the special pair

The two-dimensional photo-CIDNP MAS NMR allows for an unequivocal chemical shift assignment of the nuclei of cofactors forming the radical pair.

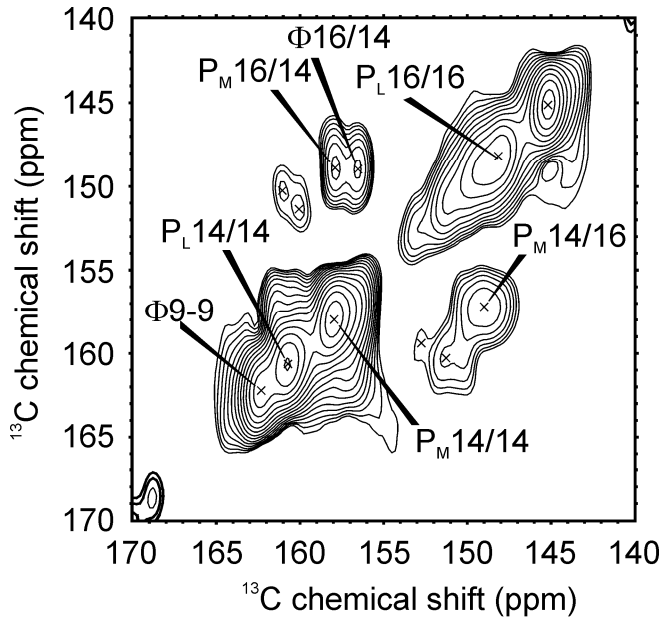

Fig. 1.14: RFDR photo-CIDNP MAS NMR 2-dimensional spectrum obtained at 200 MHz under continuous illumination. The mixing time used is 4 ms with a spinning frequency of 8 kHz at 223 K.

Since chemical shift information is related to the ground-state electronic structure, multidimensional NMR data allow mapping of electronic structures at the atomic resolution. Using RCs with selectively ^{13}C-labeled cofactors, a clear difference in the chemical shift of the electronic ground-state of the two BChl *a* cofactors forming P has been detected (Figure 1.14) (Schulten *et al.*, 2002; Prakash, 2006). Hence, the electronic symmetry of P is already broken before charge separation. Comparison to 2-dimensional MAS NMR spectra, obtained in the dark by using cross-polarization at an ultra-high field, reveals identical chemical shifts at the isotope labeled positions of the cofactors, in other words, no light induced shifts have been observed. This is in line with a low reorganization energy facilitating fast ET.

1.5.2 Entire chromatophores and cells

The enormous signal enhancement of photo-CIDNP allows studying biological units larger than isolated RC proteins. Photo-CIDNP has been observed in entire photosystem units, so-called chromatophores (Prakash *et al.*, 2003), as well as entire cells of *Rb. sphaeroides* R26 (Prakash, 2006). The method enables to study BChls of the primary donor directly in its native cellular environment at a concentration of ~100 nM without isotope enrichment. In bacterial cells, no significant changes of the electronic structure were detected in the ground-state or radical pair. Hence, isolation appears not to alter the donor side of bacterial RCs to a critical extent.

1.5.3 Photosystems of plants

In plant photosynthesis, the light-induced ET is driven by PSI and PSII. The oxidized primary electron donor of PSII, $P680^{\bullet+}$, is a very powerful oxidizing agent, whereas the electronically excited primary electron donor of PSI, P700*, is a strong reducing agent. The origin of the different redox properties and the electronic structure of both RCs is not yet clear (for review, see Webber and Lubitz, 2001; Barber, 2003; Witt, 2004). The ^{13}C photo-CIDNP MAS NMR spectra of the two plant photosystems look different in their sign patterns. As in bacterial RCs WT, in PSI preparations of PSI-110 particles all signals are emissive (Trace A in Figure 1.15) (Alia *et al.*, 2004). On the other hand, the spectrum of a D1D2-preparation of PSII appears to have a sign pattern similar to R26: the signals between 120 and 175 ppm are absorptive while the methine signals between 90 and 110 ppm are emissive (Trace B in Figure 1.15) (Matysik *et al.*, 2000; Diller *et al.*, 2005), suggesting the absence of any triplet quencher close to P680. In both spectra, there is no evidence for signal doubling in the spectrum, which is in clear contrast to the spectra of bacterial RCs. In PSI spectrum, all signals can be assigned to a single undisturbed Chl-*a* cofactor, presumably the donor cofactor. In PSII spectrum, additional broad emissive signals appear at about 140 and 130 ppm, which have been assigned to an axial histidine involved in the electronic structure of the donor (Diller *et al.*, 2007a). In PSI, an undisturbed carbonyl carbon can be observed at about 190 ppm, while in PSII the only carbonyl carbon appears surprisingly at 172.2 ppm.

An assignment of this signal to the C-13^1 carbonyl carbon would imply a chemical modification of that function (Diller *et al.*, 2005). On the other hand, this frequency is characteristic for the ester sidechain carbonyl carbons. However, from the sidechains no photo-CIDNP enhancement is expected, unless they would be localized within the π-electron cloud of the macrocycle. The responses around 100 ppm are assigned to methine carbons. It is remarkable that in the spectrum of PSII these signals have very different intensity revealing a different distribution of electron spin densities of the donor. The asymmetry in electron spin density distribution at the donor of PSII has been explained by π-π interaction with a tilted axial histidine, pulling the charge towards pyrrole rings III/IV (Diller *et al.*, 2007a). It is possible that such electronic re-organization is related to the strong shift of the redox potential of PSII (Matysik *et al.*, 2000a).

1.5.4 Relaxation measurements

Photo-CIDNP build-up and steady-state polarization depend on the spin-lattice relaxation constant T_1, since the polarization decays by longitudinal relaxation. Relaxation times T_1 have been measured using the laser setup described in Figure 1.12. A train of eighty pulses was applied in each scan in order to reach a quasi steady-state polarization. The delay between the last light flash and the detection pulse was varied from 2 s to 80 s in seven steps. Figure 1.16 shows the absolute intensities of the four most intense signals (Table 1.1) as a function of the delay. The relaxation time of approximately 17 s does not vary strongly between the different carbon nuclei. It is longer than the time constant of polarization build-up observed under continuous illumination (~4 s, Figure 1.8), which suggests that the photon rates used in the continuous illumination experiment are sufficient to saturate the system.

1.6 SCOPE OF THE THESIS

Photo-CIDNP MAS NMR is expected to further improve our understanding of ET and spin chemistry in photosynthetic RCs, especially on the exact mechanisms of electron-matrix interaction and on the precise electronic structure of the cofactors involved.

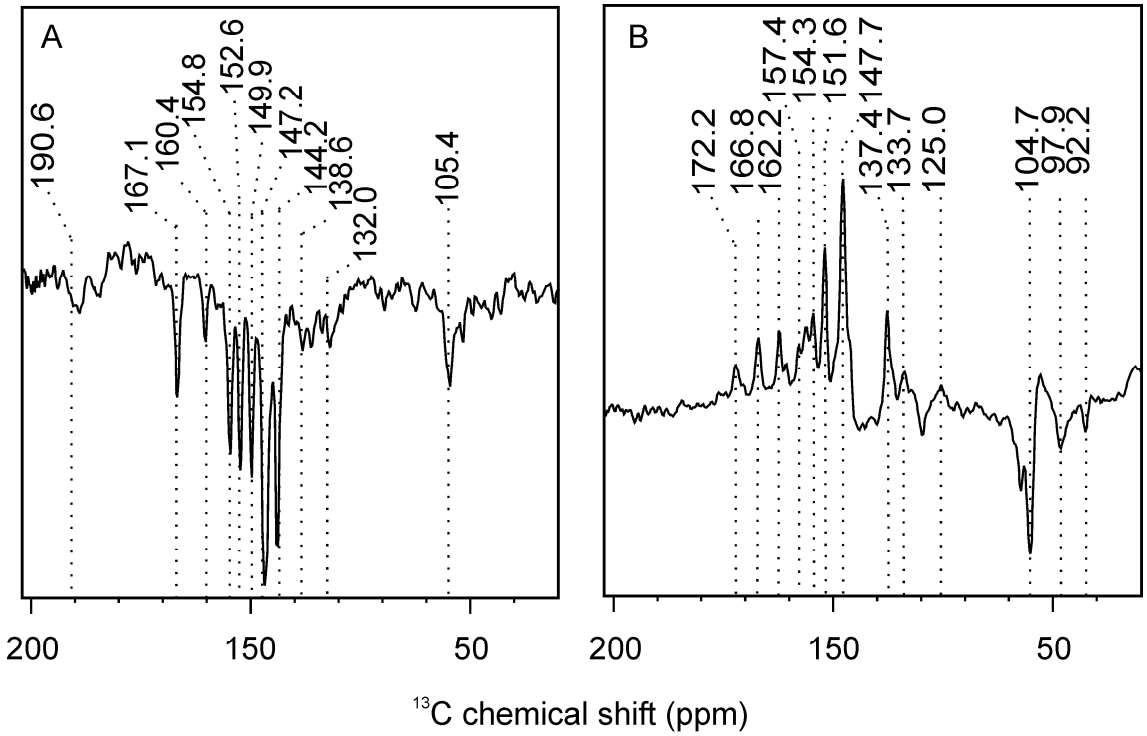

Figure 1.15: ^{13}C MAS NMR spectra of (A) PSI and (B) PSII RCs obtained under continuous illumination with white light at 223 K, in a magnetic field of 9.4 Tesla and using a MAS frequency of 9.0 kHz. Assigned resonances are indicated by the dotted lines.

Peak no.	Symbol	Chemical shift (ppm)	T_1 (s)
1	o	157.9	22.4
2	+	94.8	18.8
3	×	107.5	16.5
4	□	160.6	13.7

Table 1.1: Relaxation times T_1 for four ^{13}C photo-CIDNP MAS NMR signals (Figure 1.16).

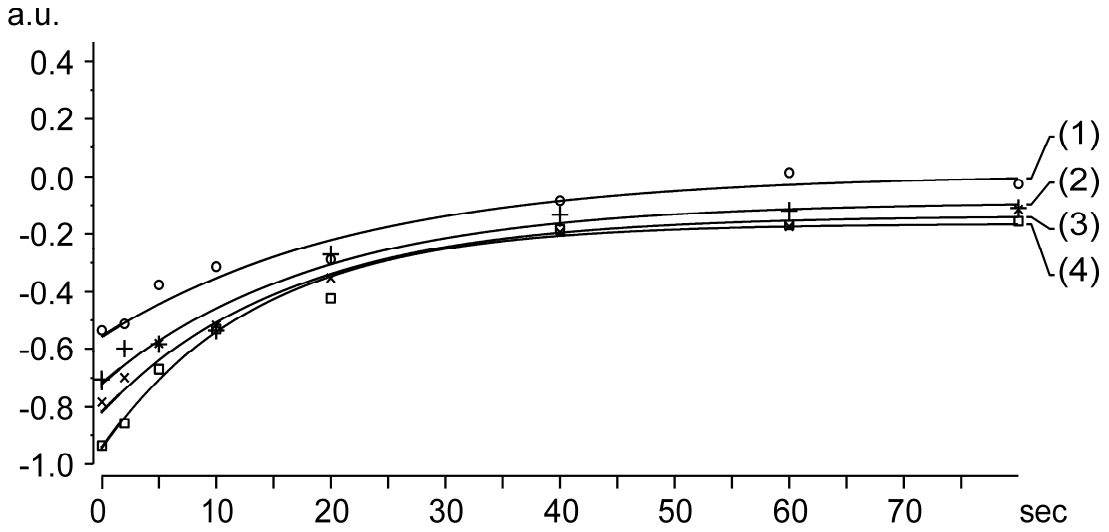

Figure 1.16: Relaxation measurement of photo-CIDNP on a [4,5,9,10,14,15,16,20-$^{13}C_8$]-BChl/BPhe labeled bacterial RC wild type. For symbols, see Table 1.1.

Until now, the solid-state photo-CIDNP effect has been observed in four natural photosynthetic systems, while experiments on artificial systems failed. It is thus possible that the occurrence of photo-CIDNP in solids is related to specific conditions of the efficient ET developed in nature. In fact, the occurrence of the DD mechanism is confined to a rather small kinetic window. Likewise, the TSM mechanism is operative only in a relatively small range of the electron-electron coupling. This and detection of the effect across a range of otherwise rather different photosynthetic RCs suggests that the occurrence of photo-CIDNP is related to an optimization of the first ET step and may thus be a guide for the improvement of artificial systems. In any case, photo-CIDNP provides an enormous potential for solid-state NMR, a method which generally suffers of a lack of sensitivity and selectivity. The solid-state photo-CIDNP effect may also provide new schemes for NMR imaging and microscopy methods.

Chapter 2 describes the setup developed for time resolved photo-CIDNP MAS NMR. In Chapter 3 the electron-nuclear spin dynamics occurring after a single photo-

cycle is described and the origin of the solid-state photo-CIDNP effect is discussed. In Chapter 4, the electronic structure of P in bacterial RC of *Rb. sphaeroides* at atomic resolution is shown. In Chapter 5, I will present general discussions and future perspectives for applications and theory development for time-resolved ns-flash photo-CIDNP MAS NMR.